HHS Public Access

Author manuscript

Neuron. Author manuscript; available in PMC 2017 June 20.

Published in final edited form as:

Neuron. 2016 July 20; 91(2): 384–396. doi:10.1016/j.neuron.2016.06.004.

Persistent Structural Plasticity Optimizes Sensory Information Processing in the Olfactory Bulb

Kurt A. Sailor[1,2,3,4,7,10], **Matthew T. Valley**[1,2,9,10], **Martin T. Wiechert**[1,2], **Hermann Riecke**[8], **Gerald J. Sun**[3,4], **Wayne Adams**[8], **James C. Dennis**[8], **Shirin Sharafi**[1,2], **Guo-li Ming**[3,4,5,6,7], **Hongjun Song**[3,4,5,7,*], and **Pierre-Marie Lledo**[1,2,*]

[1]Laboratory for Perception and Memory, Pasteur Institute, 75015 Paris, France

[2]Centre National de la Recherche Scientifique (CNRS), Unité de Recherche Associée (UMR3571), 75015 Paris, France

[3]Institute for Cell Engineering, Johns Hopkins University School of Medicine, 733 North Broadway, Baltimore, MD 21205, USA

[4]The Solomon Snyder Department of Neuroscience, Johns Hopkins University School of Medicine, 725 N. Wolf Street, Baltimore, MD 21205, USA

[5]Department of Neurology, Johns Hopkins University School of Medicine, 600 N. Wolf Street, Baltimore, MD 21205, USA

[6]Department of Psychiatry and Behavioral Sciences, Johns Hopkins University School of Medicine, Baltimore, MD 21205, USA

[7]Diana Helis Henry Medical Research Foundation, New Orleans, LA 70130-2685, USA

[8]Engineering Science and Applied Mathematics, Northwestern University, Evanston, IL 60208, USA

SUMMARY

In the mammalian brain, the anatomical structure of neural circuits changes little during adulthood. As a result, adult learning and memory are thought to result from specific changes in synaptic strength. A possible exception is the olfactory bulb (OB), where activity guides interneuron turnover throughout adulthood. These adult-born granule cell (GC) interneurons form new GABAergic synapses that have little synaptic strength plasticity. In the face of persistent neuronal and synaptic turnover, how does the OB balance flexibility, as is required for adapting to

[*]Correspondence: shongju1@jhmi.edu (H.S.), pierre-marie.lledo@pasteur.fr (P.-M.L.).

[9]Present address: Allen Institute for Brain Science, Seattle, WA 98109, USA

[10]Co-first author

SUPPLEMENTAL INFORMATION

Supplemental Information includes seven figures, six movies, and Supplemental Experimental Procedures and can be found with this article at http://dx.doi.org/10.1016/j.neuron.2016.06.004.

AUTHOR CONTRIBUTIONS

Conceptualization, K.A.S, M.T.V., M.T.W., H.J.S., and P.M.L.; Methodology, K.A.S., M.T.V., and M.T.W.; Investigation, K.A.S. (GC data), M.T.V., and S.S. (gephyrin data); Formal analysis, M.T.W and H.R. (computational model); Software, G.J.S., W.A. and J.C.D.; Writing – original draft, K.A.S., M.T.V., and M.T.W.; Writing – review and editing, K.A.S., M.T.V., M.T.W., P.M.L., H.R., G.J.S., and H.J.S.; Supervision, P.M.L., H.R., H.J.S., and G.-l.M.

changing sensory environments, with perceptual stability? Here we show that high dendritic spine turnover is a universal feature of GCs, regardless of their developmental origin and age. We find matching dynamics among postsynaptic sites on the principal neurons receiving the new synaptic inputs. We further demonstrate in silico that this coordinated structural plasticity is consistent with stable, yet flexible, decorrelated sensory representations. Together, our study reveals that persistent, coordinated synaptic structural plasticity between interneurons and principal neurons is a major mode of functional plasticity in the OB.

In Brief

Using in vivo imaging, Sailor and Valley et al. (2016) show matching, robust structural plasticity in olfactory bulb granule and mitral/tufted cell synapses. Computational modeling shows this structural plasticity is compatible with stable memory and high adaptability to changing sensory inputs.

INTRODUCTION

Synaptic plasticity, the experience-dependent modification of synaptic strength, constitutes a central paradigm of modern neuroscience to explain learning and memory at cellular and sub-cellular levels (Mayford et al., 2012). In contrast, structural plasticity, the formation of new synapses or pruning of existing synapses, remains as an alternative process of unclear significance. Structural plasticity has been linked to new memory formation in the adult neocortex (Xu et al., 2009; Yang et al., 2009), albeit with a very modest degree of synaptic remodeling. In contrast, *robust* structural plasticity mainly occurs during brain development and is temporally confined to specific postnatal critical periods (Holtmaat et al., 2005; Zuo et al., 2005). As a result, its presence in the adult brain is often assumed to be limited.

The olfactory bulb (OB) is one of a few brain regions with prominent structural plasticity (Mizrahi, 2007). In the OB, adult neurogenesis continuously replenishes two neuronal populations, periglomerular and granule cell (GC) interneurons (Alvarez-Buylla and Lim, 2004; Lois and Alvarez-Buylla, 1994; Whitman and Greer, 2009), making the OB a compelling model to address how a neural circuit with substantial structural plasticity can maintain stable function.

GCs are GABAergic, axonless interneurons that constitute the largest group of neurons in the OB (Shepherd et al., 2007). They make specialized dendrodendritic synapses with mitral/tufted cells (MC/TCs), the principal relay neurons of the OB (Lepousez et al., 2013; Rall et al., 1966). This bidirectional synaptic structure conveys both MC/TC excitatory glutamatergic input onto GCs and reciprocal GABAergic output onto MC/TCs (Shepherd, 1963).

The development of adult-born GCs has been tracked by histological (Petreanu and Alvarez-Buylla, 2002), physiological (Carleton et al., 2003), in vitro (Breton-Provencher et al., 2014), and in vivo imaging methods (Mizrahi, 2007). Chronic in vivo imaging has revealed the dynamic stages of periglomerular neuron dendrite and GC dendritic tip development (Mizrahi, 2007), but the developmental stages of complete GC dendrites in vivo remains

uncharacterized. GC spine dynamics have also been tracked up to a cell's age of 3 months, exhibiting ~20% daily turnover (Mizrahi, 2007). However, it is unclear if GC spine dynamics, like plasticity of synaptic strength elsewhere in the brain, are restricted to defined critical periods and stabilize with increasing GC age. Similarly, it is unknown if highly dynamic spines are limited to adult-born GCs, or instead are universal to all GCs.

Highly dynamic GC spines beg the question of whether synaptic reorganization is mirrored by the MC/TC GABAergic postsynaptic structure. In neocortical pyramidal neurons, GABAergic postsynaptic sites have greater dynamics compared to excitatory synapses (Chen et al., 2012; Villa et al., 2016). Therefore, it is possible that MC/TC synapses have similar plasticity. Alternatively, if the MC/TC postsynaptic GABAergic structure is instead stable, this would suggest GC competition for limited synapses.

Plasticity in neural circuits must strike a balance between flexibility and stability so new information can be acquired while previously learned information can be retained (Fusi et al., 2005). This is especially relevant in sensory systems where the representation of a dynamic environment has to be adaptable, yet reliable. Here, we approached this conundrum by tracking the complete development of adult-born GCs using chronic in vivo two-photon imaging, comparing GC spine dynamics to the dynamics of the postsynaptic GABAergic sites on MC/TCs. Finally, we developed a computational model, based on our experimental results, to explore the functional outcomes of ongoing structural plasticity in the OB. Our results strongly suggest an adult brain circuit that utilizes structural plasticity as its primary form of functional plasticity.

RESULTS

For characterizing the complete structural stages of adult-born GC development in vivo, cells were birth-dated and labeled with GFP by injecting GFP-expressing virus into the subventricular zone (SVZ), the location of neuroblast proliferation (Figure 1A). Labeled neuroblasts migrated via the rostral migratory stream (RMS) to the OB, where two-photon imaging was performed through a cranial window. The birthdating of adult-born neurons was confirmed by immunohistological analysis. Doublecortin (DCX)-positive GFP neuroblasts appeared in the posterior RMS up to 7 days postinjection (dpi) but were absent by 14 dpi, demonstrating pulsed labeling of a cohort of neuroblasts (see Figure S1A available online). By 42 dpi, the cells differentiated with a GC morphology and expressed a mature neuronal marker (Figure S1B).

Cranial windows were made over the OB, and blood vessel patterns remained stable for over 2 months after surgery (Figure S1C). To determine the potential invasiveness of the cranial window surgery (Lee et al., 2008; Xu et al., 2007), the OB was stained for markers of gliosis (GFAP) and microglia (Iba-1) in no-window controls, at 14 and 28 days after window surgery, and 10 days after "failed windows," serving as a positive control (Figure S1D). Quantification of the immunofluorescence showed no change in Iba-1 immunoreactivity (Figure S1E) but a significant increase in GFAP (Figure S1F) in 14 days after window surgery and failed window groups. There was no statistical difference in GFAP between no-window and 28 days postwindow groups ($p = 0.25$). To insure minimal impact of the surgery

on OB physiology, all imaging series started at least 1 month after cranial window surgery (Holtmaat et al., 2009).

Adult-Born GC Dendrites Elaborate in a Stereotypical Manner

To track the initial integration events of newborn GCs arriving into the OB, experiments were performed as outlined in Figure 1B. Two-photon image stacks were acquired every 2 days (Movie S1) from first detection of cells (~12 dpi). The same GCs were traced in 3D over multiple time points, showing the evolution of their morphology with synaptic integration (Figure 1C). Given the heterogeneity in neuroblast arrival times to the OB (Petreanu and Alvarez-Buylla, 2002), each individual GC was time normalized at the dpi where the total dendritic length initially plateaued (23.2 ± 1.4 dpi; hereafter all values indicate mean ± SEM). Additionally, there was high diversity between individual GCs in their mature total dendritic lengths, therefore each GC was normalized with 100% being the individual dendritic length average between 36 and 58 dpi (Figure 1D, average 902.9 ± 62.4 μm). GCs had a mean growth rate of ~12% of their saturated length per day (Figure 1E, n = 3 animals, 14 GCs and 174 tracings).

Scholl analysis was performed showing an initial suggestion of dendritic overshoot at ~24 dpi, with refined stability by 30 dpi (Figures S1G and S1H). The total dendritic length remained highly stable after 1 month postinjection (mpi), in addition to individual dendritic segments becoming stable (Figures 1F and 1G, n = 3 animals, 13 dendritic segments, and 210 tracings). The adult born GC population was also tracked with the highest number of cells existing at 24 dpi, peak cell death occurred at 26 dpi (~2.5% loss/day) and from 24 to 56 dpi, the total cell number declined at ~0.7% per day (n = 2 animals, 85 cells; 24–56 dpi linear fit $R^2 = 0.96$).

Spine Dynamics of Adult-Born GCs Evolve during Integration and Saturate

Using the same experimental timeline as in Figure 1B, GC spine dynamics were tracked. The first spines appeared at ~18 dpi (Figure 2A; 17.9 ± 1.0 dpi), similar to observations in fixed brain sections (Petreanu and Alvarez-Buylla, 2002). GC dendritic segments and spines were traced in 3D to track dynamic changes (Figures 2B and S2A–S2C). The number of new spines was highest during the initial stage of GC dendrite formation, up to 1 mpi (Figure 2C, n = 11 animals, 23 dendritic segments, 253 tracings, and 3,638 spines). After this period, the number of new and of lost spines decreased, while that of stable spines gradually increased. Three phases were binned at 22–30, 40–48, and 64–72 dpi, showing a significant increase in stable spines and a gradual decrease in new and lost spines with increasing age of the adult-born GCs (Figure 2D, 22–30 dpi: stable, 33.5% ± 1.2%, new, 33.7% ± 1.3%, lost, 32.9% ± 0.7%, n = 4 animals, 10 dendrites, 37 tracings and 832 spines; 40–48 dpi: stable, 48.0% ± 1.6%, new, 25.2% ± 1.3%, lost, 26.8% ± 1.0%, n = 9 animals, 16 dendrites, 60 tracings and 807 spines; 64–72 dpi: stable, 59.7% ± 2.6%, new, 20.3% ± 1.4%, lost, 20.0% ± 1.3%, n = 3 animals, 4 dendrites, 20 tracings, and 274 spines; stable 22–30 versus 40–48 dpi $p = 1.5 \times 10^{-11}$, 40–48 versus 64–72 dpi $p = 1.8 \times 10^{-5}$; new 22–30 versus 40–48 dpi $p = 1.8 \times 10^{-5}$, 40–48 versus 64–72 dpi p = 0.06; eliminated 22–30 versus 40–48 dpi $p = 1.5 \times 10^{-3}$, 40–48 versus 64–72 dpi $p = 9.8 \times 10^{-3}$; ANOVA). Time-averaged overlay images of the developmental periods showed a gradual increase in stable spines, but generally a very

dynamic mix of short-lived spines persisted (Figure 2E; Movie S2). Overall, the percentage of dynamic spines consisted ~40% of the population at 2 mpi. A control experiment confirmed the rapid spine turnover was not the result of repeated 2-day interval, anesthetized imaging (Figures S2D–S2F).

Adult-Born GC Spines Maintain High Structural Plasticity throughout Life

Are the high dynamics of dendritic spines on adult-born GC maintained throughout the life of a given cell? GC precursors were labeled as outlined in Figure 3A. In addition, cranial windows were made over the motor cortex of Thy-1-GFP-M mice to compare directly spine dynamics of neocortical pyramidal cells and adult-born GCs. Spine stability, as a function of GC age, saturated at ~2 mpi with ~60% stability (Figures 3B and 3C, data combined with Figure 2D, first three time point values; 3 mpi: 57.5% ± 2.0%, n = 3 mice, 12 dendrites, 60 tracings and 624 spines; 4 mpi: 58.8% ± 1.8%, n = 3 mice, 7 dendrites, 26 tracings and 349 spines; 6 mpi: 61.0% ± 1.7%, n = 3 mice, 7 dendrites, 18 tracings and 232 spines; 14 mpi: 66.8% ± 2.6%, n = 3 mice, 7 dendrites, 14 tracings and 183 spines; Thy-1-M: 98.8% ± 0.4%, n = 2 mice, 23 dendrites, 52 tracings and 142 spines; 22–30 dpi versus all mpi $p < 0.01$, 40–48 dpi versus all mpi $p < 0.05$, 14 mpi versus neocortex $p = 1.2 \times 10^{-9}$, ANOVA). From 2 to 14 mpi, the spines were significantly more stable than spines at 1 and 1.5 mpi. Between 3, 4, 6, and 14 mpi groups, despite a gradual trend toward higher stability with the age of the GC, the stability was not significantly different. Additionally, adult-born GC spines were consistently more dynamic than adult neocortical pyramidal cell spines (Figure 3C). These results indicate that adult-born GC spines likely retain elevated dynamics throughout the cell's life.

Using a 2-day interval imaging undersampled faster spine movement, therefore we also imaged 3, 5, and 18 mpi GCs and adult neocortical pyramidal cells at a 10 min interval (90 min total, Figure S3). GCs had numerous highly dynamic spines with a filopodia-like morphology (Figure S3B, open arrowheads 1, 2, and 4). Additionally, mushroom-like spines had fine dynamic protrusions on established spine heads (Figure S3A, open arrowhead 1). Even in 18 mpi GCs, these highly motile structures were observed (Figure S3C). Enhanced short-term spine dynamics were ubiquitous in all observed GCs (Movie S3) and were absent in neocortical pyramidal cell spines (Figure S3D; Movie S4). Quantification of spines that showed significant morphological change during the 90 min period (new, lost, or filopodia-like extensions off of existing spines), showed a similar rate with the 2-day interval results, having 66.0% ± 4.3% stable and 34.0% ± 4.3% dynamic spines, indicating a relatively constant rate of gain and loss (n = 3 animals, 12 dendrites, and 344 spines).

Adult-Born and Early Postnatal-Born GCs Exhibit Identical Rate of Spine Turnover

The OB undergoes latent development with most growth occurring within the early postnatal period and plateaus by adulthood (Pomeroy et al., 1990). Previous studies demonstrated adult-born GCs to have unique properties in comparison to the early postnatal-born GC population (Alonso et al., 2012; Lemasson et al., 2005; Valley et al., 2013). We therefore explored whether dynamic spines were restricted to adult-born GCs. Postnatal day 14 (P14) mice were injected with the same GFP-expressing virus, along with a cohort of mice injected at postnatal day 70 (P70) for labeling adult-born GCs as outlined in Figure 4A.

When comparing the spine dynamics between the adult and early postnatal-born GCs, there was ~60% stability at a 2-day interval, which was not statistically different between groups (Figures 4B and 4C; P70: n = 4 mice, 19 dendrites, 973 spines, stable: 58.0% ± 1.4%, new: 21.9% ± 1.2%, lost: 20.1% ± 1.3%; P14: n = 4 mice, 14 dendrites, 522 spines, stable: 58.2% ± 2.7%, new: 22.5% ± 1.7%, lost: 19.3% ± 1.5%; P70 versus P14 stable: p = 0.94, new: p = 0.81, lost: p = 0.74, ANOVA). These results suggest that all GCs, irrespective of their origin, have highly dynamic spines throughout life.

Postsynaptic Dynamics of Gephyrin in Principal OB Neurons

The high amount of GC spine turnover could require matching plasticity in the postsynaptic site along the MC/TC lateral dendrite, or alternatively, GC spines may compete for fixed synaptic sites. We monitored GABAergic post-synaptic sites by two-photon in vivo imaging of fluorescently tagged gephyrin (teal-gephyrin; Figure 5A), an obligate scaffolding protein enriched at GABAergic synapses (Specht et al., 2013; Tyagarajan and Fritschy, 2010). Lentiviral vectors that conditionally expressed teal-gephyrin were injected directly into the OB of cre-driver mice (Tbet-Cre) (Haddad et al., 2013) to target expression to MCs and TCs (Figure 5B), the only output neurons in the OB. Imaging the volume in the injection area revealed sparse expression, which enabled reconstruction of neuronal morphology (Figure 5C). All fully reconstructed neurons had the morphological characteristics of MC/TCs: primary dendrites that branched into single glomeruli, and multiple spineless secondary dendrites with broad axial ramifications in the external plexiform layer (Figures 5E and 5F). Consistent with previous in vivo observations, we found no evidence of dynamics in the MC/TC dendritic structure (Mizrahi and Katz, 2003). From in vivo z stacks (n = 7 mice), 38 reconstructed neurons were classified as either MCs (n = 20) or TCs (n = 18) based on somatic depth (Figure 5D).

To determine if teal-gephyrin was enriched at synapses, we quantified the immunohistochemical colocalization of teal-gephyrin with endogenous synaptic proteins. It was previously reported that $GABA_A$ receptors on MCs and TCs contain the alpha-1 subunit of the $GABA_A$ receptor and not the alpha-2 sub-unit (Panzanelli et al., 2007). As expected, we found that in MC/TCs teal-gephyrin puncta colocalized with the alpha-1 (Figures S4A and S4C) but not the alpha-2 $GABA_A$ receptor subunit (Figures S4B and S4C).

MC/TCs lack morphologically distinct postsynaptic structures such as spines that can experimentally assist the identification and registration of postsynaptic fluorescent labels (Chen et al., 2012; van Versendaal et al., 2012). Therefore, to track the dynamics of puncta over multiple days of observation, we developed an automated workflow to detect postsynaptic puncta on smooth dendrites from a time series of two-photon imaged volumes (Figure S5). We discriminated between real puncta movement versus nonbiological optical changes by comparing images acquired at 10 min intervals—a scale with negligible gross rearrangement to gephyrin assemblies (Dobie and Craig, 2011) (Figure S5A)—and 1-day intervals (Figure S5B; quantified in Figure S5C). We measured a similar rate of gain and loss over four 10 min observations (Figures S5D and S5E) which contrasted with significantly larger changes between 1-day interval observations over a period of 4 days (Figures S5D and S5E). Our algorithmic detection of puncta dynamics was robust to

changes in various detection parameters (Figures S5F and S5G) and was validated by human scoring (Figure S5H).

Inferring the Age of New and Lost Gephyrin Puncta

Puncta were classified by age (Figure 6A). Our dataset is marked by puncta at, or near, the optical point spread function of the microscope where the size of the gephyrin scaffold is best reflected by puncta intensity. As a result, we looked at the peak intensity of teal-gephyrin puncta in order to gain insights regarding the age and strength of the synapses that were gained and lost. We found that the peak intensity of newly-formed puncta was initially dim and increased over time (Figure 6B; Movie S6), whereas stable puncta were considerably brighter and did not change intensity over 8 consecutive days of observation (Figures 6B and 6C). Because the short lifetime of dim puncta could be explained by the increased likelihood of dim puncta to disappear below the threshold of detection, we repeated our analysis using different detection thresholds (also see Figures S5F and S5G) but found no change in the slope or half-max of the logistic fit (½ max: 0.5% threshold, 6.1 ± 0.2 days; 1.0% threshold, 5.7 ± 0.3 days; 2.0% threshold, 6.0 ± 0.3 days; mean ± SE, Figure 6C). Logistic growth of puncta intensity suggests that gephyrin recruitment to the post-synaptic density saturates over several weeks, which may indicate a time dependence of synaptic strength following synaptogenesis.

In our dataset, 64% of lost puncta (1,222/1,899) were pre-existing, meaning they were observed from the first day of imaging. This subpopulation of lost pre-existing puncta was significantly brighter than puncta that were gained and then lost (36%, 677/1,899) during the imaging session (mean peak intensity: lost pre-existing, 87.3 ± 42.6; lost new, 40.0 ± 36.4; Mann-Whitney $p < 1.0 \times 10^{-4}$). The lost pre-existing population of puncta had on average 76% the peak intensity of stable puncta (stable puncta peak intensity; 115.1 ± 52.4, n = 7125 puncta), indicating that puncta loss was not restricted to a young dynamic fraction, and instead many stable long-lived puncta were subject to elimination.

MC/TC Gephryin Puncta Dynamics Mirror GC Spine Dynamics

To estimate the overall dynamics of gephyrin puncta, we focused our analysis on puncta that persist for two or more observations to exclude spurious false positives resulting from our automated detection. The 10 min observation gain/loss was used as a baseline to calculate the real turnover in different types of dendrites. We chronically imaged volumes for 4–8 consecutive days and extracted 56 dendrite segments from MC and TC secondary dendrites (30 MC segments, 26 TC segments; mean length: 77.8 ± 19.7 μm; average 50.4 ± 29.0 puncta per segment). Both groups exhibited a similar 1-day interval rate of puncta addition (% new puncta per day: TC, 7.0% ± 3.6%; MC, 6.1% ± 4.6%; p = 0.42; Figure 6D), puncta loss (% lost puncta per day: TC, 7.0% ± 3.4%; MC, 6.0% ± 3.4%; p = 0.30; Figure 6D) and puncta stability (% stable puncta per day: TC, 86.0% ± 0.9%; MC, 87.9% ± 1.2%; p = 0.22; Figure 6D). To correlate puncta with GC spine dynamics, single observation spines were also excluded. We found no statistical difference between the MC/TC puncta and GC spine dynamics, suggesting matched dynamics between the synaptic partners (n = 4 mice, 22 dendrites and 463 spines, % GC new spines per day: 5.1% ± 0.9%; p = 0.12 versus MC/TC;

% GC lost: 5.7% ± 1.0%; p = 0.40 versus MC/TC; % GC stable: 89.2% ± 1.0%; p = 0.18 versus MC/TC; ANOVA; Figure 6D).

Functional Consequences of Persistent Structural Plasticity

What is the function of high synapse turnover, and how can a persistently remodeled OB output stable sensory representations? We addressed these questions in a linear rate model (Figure 7A). Model MCs (N_{MC} = 120) were driven by odor-evoked glomerular activation maps (Johnson and Leon, 2007) and excited GCs (N_{GC} = 2,000), which returned reciprocal inhibition. To reproduce the experimentally observed synapse turnover, the MC end of a subset of the reciprocal synapses was replaced every Δt = 3 hr. We first implemented a minimal update rule: random replacement at a constant rate ("Poisson model").

The OB transforms its inputs into reformatted MC output patterns. Using Pearson's distance (Figure 7B), we therefore quantified how much model output differed from input for a set of 12 odors (the "odor environment") and rejected models with too small I/O-distance $d_{I/O}$ < 0.05. Background synaptic plasticity can degrade stored memory (Fusi and Abbott, 2007; Fusi et al., 2005). Indeed, the Poisson model erased any initially stored I/O function (See Supplemental Experimental Procedures) within a few simulated days and always evolved toward a random configuration ("Poisson network") with $d_{I/O}$ < 0.032 (n = 1440/1440 = 36 stimuli × 40 circuits; Figures 7C and S7A).

Older Synapses Are More Stable

Since the Poisson networks' failure to reshape their inputs is at odds with known OB properties (Friedrich and Laurent, 2001; Gschwend et al., 2015), we reanalyzed the experimental data. For a homogeneous Poisson process, which is context and history agnostic, the replacement rate of a synapse would be independent of its age. We analyzed spines of mature GCs over 12 days (seven 2-day interval sessions). Spines not observed at the first session were classified as young. At each session each young spine was assigned an age according to the number of consecutive sessions in which the spine was previously detected. When branches were pooled, the 2-day survival rate, i.e., the probability still to be observed at the next session, increased significantly with spine age (Figure 7D, colored bars; p = 3.0×10^{-3}, Spearman's rank correlation coefficient). Corroborating this trend, the 2-day survival rate of young spines was less than that of all spines for each individual branch in the data-set (n = 13; Figure S7B). MC/TC puncta showed the same trend (Figure S7C; p = 3.0×10^{-3}, Spearman's rank correlation coefficient), with smaller effect size, possibly due to the shorter total observation period. In summary, synapse stability increased with GC spine and MC/TC puncta age.

Hebbian, Activity-Dependent Survival Stabilizes Older Synapses

Differential survival rates may originate from the maturation or heterogeneity of synapses, or from modulatory factors such as neuronal activity. The latter is suggested by reduced turnover in odor-enriched conditions (Livneh and Mizrahi, 2012). We therefore built a new model with activity-dependent synapse survival.

At each time step, the product of the responses of any connected MC-GC pair was calculated for each odor in the environment. Because these products are large for cells that fire together, their sum over all odors measures the Hebbianness of the connection, and a running average defined the “resilience” of the synapse. In the subsequent connectivity update, low-resilience synapses were more likely to have their MCs replaced with randomly chosen other MCs (Figure S7D). This “Hebbian model” showed continual synapse turnover and, for suitably chosen parameters, reproduced the observed increase in synapse stability with synapse age with high accuracy (Figure 7D, gray bars).

Hebbian Networks Generate Stable Stimulus Representations

Odor experience shaped “Hebbian networks” that, unlike Poisson networks, consistently transformed their inputs (steady-state $d_{I/O} = 0.206 \pm 0.004$, mean ± SEM, n = 336 = 24 odors × 14 circuits; Figure 7B). However, because of the highly volatile circuit connectivity, it was unclear whether output odor representations were stable. We quantified output stability using the Pearson correlation r_{64} between the response vectors at times t and t-64 days. For fixed olfactory environment, GC responses strongly fluctuated throughout the simulation (Figure 7E, blue trace). By contrast, after an initial transient, MC output reliably stabilized with r_{64} near unity (Figure 7E, black trace).

How can a volatile circuit generate stable output? Two troughs flanking the central peak of the average autocorrelation of MC response time courses (Figure S7E) hinted at a negative feedback loop counteracting temporal fluctuations. Suggestively, the temporal waveforms of the MC response and of the number of GC synapses received by the same MC, which was proportional to GC-mediated inhibition, were highly anticorrelated (average Pearson correlation: $r < -0.99$). The average cross-correlogram between MC response and average resilience of connected synapses (Figure S7F) suggested that an increased MC response enhances the resilience and thus the number of connected synapses. The resulting added inhibition rebalances the MC response. This negative feedback loop also compensated partially for slow fluctuations in input representations (Figures 7F and S7G), which may, for example, result from olfactory receptor neuron (ORN) turnover (Graziadei and Graziadei, 1979). By contrast, in the Poisson model, synaptic fluctuations exacerbated input fluctuations. Thus, despite the volatility of input and connectivity, Hebbian, but not Poisson, plasticity kept output representations stable.

Hebbian Networks Decorrelate Stimulus Representations

GABAergic activity is pivotal to several OB computations (Lledo and Lagier, 2006). Among these, pattern decorrelation enhances odor discrimination in the early learning phase (Gschwend et al., 2015), and facilitates presumed downstream computations (Friedrich and Wiechert, 2014; Gschwend et al., 2015; Wick et al., 2010; Wiechert et al., 2010). To probe whether spine turnover and pattern decorrelation may be related, we exposed the Hebbian model to a 12-odor environment. MC representations adapted reliably, substantially reducing the average output pattern correlation between pairs of similar odors (input Pearson correlation > 0.6; Figures 7G, S7H, and S7I). In a series of models with gradually relaxed selectivity of the Hebbian rule (see Supplemental Experimental Procedures), the age

dependence of spine survival and the decorrelation of odor representations decreased in parallel (Figure S7J).

Stimulus Features that Determine Network Structure

Does the Hebbian network adapt to specific features of the odor environment? For each glomerulus, we collated the vector of ORN responses to each odor in the environment. Given a pair of MCs and associated glomeruli, the similarity of these “response profiles” (Figure 7H) predicted the weight of mutual disynaptic inhibition between the MCs (Figure 7I, top) in the Hebbian (Figure 7J, black dots; $r = 0.678$) but not the Poisson model (Figure 7I, bottom; Figure 7J, gray dots; $r = -0.055$). This elevated mutual inhibition between similarly tuned MCs suggests a decorrelation mechanism similar to that in Chow and colleagues’s work (Chow et al., 2012).

DISCUSSION

Using in vivo imaging of the OB, we characterized the development of adult-born GCs, the dynamics of adult-born versus early postnatal-derived GC spines, and the dynamics of their synaptic partners. We found that all GCs retained highly dynamic spines, independent of their origin, and these dynamics were mirrored by gephyrin puncta turnover in MC/TC postsynaptic partners. Despite these high dynamics, our modeling demonstrates that a structurally dynamic network can maintain stable odor representations while also allowing the circuit to reliably adapt to novel odor environments.

Adult-Born GC Dendritic Integration and Stability in the OB

For the first time, we show in vivo the complete development of individually tracked adult-born GCs. Previous in vivo studies concentrated on more superficial OB structures, measuring changes in periglomerular neuron dendrites and cell turnover along with GC distal dendritic segments and spines, including glutamatergic synaptic puncta changes (Adam and Mizrahi, 2011; Kopel et al., 2012; Livneh and Mizrahi, 2012, 2011; Mizrahi, 2007; Mizrahi et al., 2006). The complete GC structure, however, had not been tracked.

Adult-born GC dendritic development has also been characterized histologically using a population average to cluster dendritic morphology into five developmental stages (Petreanu and Alvarez-Buylla, 2002). Due to variable neuroblast migration times to the OB, this approach entails a blurring of birth dates. In vivo imaging allowed us to detect the arrival of each individual immature GC into the OB (~10–28 dpi), providing greater accuracy in tracking morphological changes. With histological methods, the first cells were shown to enter the OB between 7 and 13 dpi as class 2 cells (Petreanu and Alvarez-Buylla, 2002). We first detected fluorescent cells in the OB at 10 dpi, later than with histological methods. This difference is likely due to the GFP fluorescence being weak in very immature cells, coupled with the cells’ deep location in the OB (>500 μm), causing it to be below the in vivo imaging detection threshold.

We observed a ~12% growth per day of the GC dendrites with the maximum length plateauing at ~23 dpi. Thereafter, the dendritic structure remained stable up to 60 dpi. These results suggest a stereotypical sequence driving GC morphological changes to maturity,

similar to that observed in adult-born neurons in the hippocampus in vivo and with serial reconstruction imaging (Gonçalves et al., 2016; Sun et al., 2013). Synaptic inputs to the GC basal dendrites, primarily from top-down centrifugal fibers and MC/TC collaterals, become active at 10 dpi, and this activity may drive the maturation steps (Kelsch et al., 2008; Whitman and Greer, 2007). In contrast, in periglomerular neurons, sensory deprivation at 10 dpi had no effect on dendritic maturation (Mizrahi, 2007), whereas odor enrichment caused a doubling in the total dendritic length of the periglomerular neurons in enriched zones (Livneh et al., 2009). Further in vivo studies with activity manipulation during dendritic development would be of great interest to determine how strongly activity drives dendrite maturation.

We also tracked GCs with a peak in total number at 24 dpi, a maximum in cell death at 26 dpi, and a gradual 0.66% per day decline in total GCs. These results may appear to contrast previous studies utilizing bromodeoxyuridine (BrdU) where total cells peaked at 15 dpi with half disappearing by 1 month (Mouret et al., 2008; Winner et al., 2002). BrdU histology has higher sensitivity compared in vivo imaging of GFP-labeled cells, thus we had a lower probability of detecting faint, deep neuroblasts. Therefore, our in vivo results suggest that cell death mainly occurs before neuroblasts elaborate and differentiate into GCs. We did observe the disappearance of fully matured GCs, albeit this occurred rarely.

GC Spines Are Highly Structurally Plastic Irrespective of Their Origin and Age

We imaged the evolution of spine dynamics as GCs developed to beyond 2 months of age. The spines were first (22–30 dpi) highly motile with comparable dynamics between new, stable, and eliminated spines. Beyond 30 dpi, spines gradually stabilized. Interestingly, this timing correlates with the formation of the first functional GABAergic output of adult-born GCs (Bardy et al., 2010). By 60 dpi, the spine dynamics saturated to 60% stability at a 2-day interval, in agreement with previous in vivo studies (Kopel et al., 2012; Mizrahi, 2007). These matching results are also important since we used oncoretrovirus for GFP expression, whereas the previous studies used lentivirus, indicating the choice of virus had no effect on the dynamics.

In our study, we show for the first time that these dynamics were sustained (>14 mpi) and thus essentially exist throughout the life of the GC. This highly dynamic state is unique when compared to our observation of pyramidal cell spines in neocortex, which had highly stable spines. Other studies demonstrated neocortical pyramidal cell spines to have a 1%–2% turnover at a 3-day interval (Grutzendler et al., 2002). To contrast brain regions, a turnover of 25% of spines, as occurs in less than 2 days in the OB, took 18 months in neocortical pyramidal cells (Zuo et al., 2005).

Adult-born GCs differ in many respects from GCs formed during development. Their somas are clustered deeper in the GC layer (Lemasson et al., 2005), they have a distinct pattern of synaptic integration into the OB compared to early post-natal-born GCs (Kelsch et al., 2008), they exhibit distinct survival rates (Lemasson et al., 2005), and their GABAergic output exhibits less synaptic depression (Valley et al., 2013). In addition, adult-born GC survival is sensitive to olfactory learning (Mouret et al., 2009) and has a role in perceptual learning (Moreno et al., 2009), long-term memory (Lazarini et al., 2009), and fear

conditioning (Valley et al., 2009). Finally, specific stimulation of adult-born GCs enhanced olfactory learning (Alonso et al., 2012). Our results show, however, that robust structural plasticity is common to early postnatally and adult born GCs: both retain highly dynamic spines throughout life. With the regular influx of new GCs into the OB, it is conceivable that the entire GC population must be highly dynamic to be compatible with synaptic integration of the new adult-born population. Similar heightened dynamics were reported in pyramidal cells of the developing cortex (Holtmaat et al., 2005; Zuo et al., 2005). Thus, the adult OB may operate in a persistently immature state. Interestingly, CA1 neuron spines were found to have higher dynamics than within neocortex, showing diversity in structural plasticity between brain regions (Attardo et al., 2015). Since the hippocampus undergoes adult neurogenesis within the dentate gyrus, neuronal circuits associated with neurogenic regions may have heightened structural plasticity.

MC/TC Gephyrin Puncta Are Highly Dynamic along Lateral Dendrites

When structural remodeling of synaptic connections occurs in cortical regions, dynamics are observed in both axonal boutons and dendritic spines (De Paola et al., 2006; Knott et al., 2006; Zuo et al., 2005). In these regions, neither pre- nor postsynaptic cells undergo replacement through adult neurogenesis, and so synaptic dynamics likely function to remap connectivity. In contrast, in the OB, neuronal turnover through adult neurogenesis forces some rate of synapse loss. Thus, the dynamics in the OB may reflect the re-establishment of specific synaptic connectivity. Without observing paired dynamics between M/T and GCs, we cannot directly assess if circuit connectivity is remapped. However, in the absence of a plausible mechanism to tag and reconnect GCs and M/Ts, matched dynamics likely reflects the establishment of new connectivity.

If structural dynamics remap GABAergic connectivity in the OB, what leads and regulates this process? While we propose it is unlikely to be random and may be regulated by a Hebbian rule (see below), it is unclear what this means mechanistically. Possibly, incoming sensory excitatory activity may stabilize specific spines (Livneh and Mizrahi, 2012). Alternatively, GCs may lead structural dynamics, which could be determined by simultaneously imaging GABAergic release machinery and PSD-95 post-synaptic scaffolds, similar to what was recently demonstrated in sensory cortex (Villa et al., 2016). Ultimately, untangling the sequence of dynamic changes at the GC-MC/TC reciprocal synapse may require new technical innovations, including maturing super-resolution imaging techniques in vivo, and developing a wider toolbox of spectrally separable synaptic labels.

Cortical interneuron classes may project GABAergic synapses onto spatially restricted subdomains of the principal neuron dendritic arbor (DeFelipe, 1997; Karube et al., 2004; Markram et al., 2004; Somogyi et al., 1998). In contrast, we found no evidence that GCs concentrate their GABAergic output to specific subregions of the MC/TC lateral dendrite (e.g., near-somatic versus distal) in contrast to a previous report (Bartel et al., 2015), and we found no difference in dynamics in different compartments. Nonetheless, our spatially restricted analysis cannot rule out higher-order patterning of turnover, such as clustered turnover dynamics and intermittent turnover at the same location, as described in mouse cortex (Chen et al., 2012; Villa et al., 2016).

At the molecular scale it remains unclear what underlies the dynamics we observed among teal-gephyrin puncta. Gephyrin rafts can undergo diffusive or coordinated movement, and they can fracture or combine (Dobie and Craig, 2011). Similarly, $GABA_A$ receptors undergoing surface diffusion from extrasynaptic sites can be trapped by gephyrin densities (Bogdanov et al., 2006; Meier et al., 2001; Triller and Choquet, 2005). Postsynaptic scaffold proteins may gradually accumulate following synaptogenesis, resulting in a correlation between postsynaptic morphology and synapse lifetime (Cane et al., 2014; van Versendaal et al., 2012; Yasumatsu et al., 2008). Both pre- and postsynaptic size can also be modified during synaptic plasticity as a means of increasing synaptic strength (Bannai et al., 2009; Bourne and Harris, 2012), and the size of the post-synaptic gephyrin density has been shown to directly relate to the number of receptors docked in the membrane (Specht et al., 2013), thus determining GABAergic quantal strength (Nusser et al., 1997). Our data suggest that gephyrin puncta age correlates with synaptic size and, by extension, synaptic maturity and synaptic strength. In addition, we found that puncta intensity did not predict puncta loss. Therefore, as with spine dynamics, post-synaptic remodeling does not appear to be a feature exclusive to young, immature synaptic contacts. It remains to be seen whether gephyrin dynamics on M/T cells can be modulated in an activity-dependent fashion, as has been observed previously (Bannai et al., 2009).

OB Structural Plasticity Supports Stable Odor Representations and Adaptive Decorrelation

We observed synapse dynamics that systematically deviated from a homogeneous Poisson process but were well reproduced by a Hebbian learning rule. In our modeling this rule led to stable output representations and substantial pattern decorrelation. The likely mechanism underlying pattern decorrelation requires GCs to connect specific MCs whose identities depend on unpredictably emerging relevant stimuli. We propose that the unusually high level of structural plasticity in the OB may enable GCs to efficiently find and connect to MCs with similar response profiles. Moreover, since this structural plasticity occurs over just a few days, it may also be utilized in olfactory perceptual learning where the network is required to adapt to changes in odor environment (Moreno et al., 2009).

Structural Plasticity May Be the Dominant Form of Plasticity in Dendrodendritic Synapses

Evidence for long-term potentiation (LTP) in the dendrodendritic synapse is lacking (Dietz and Murthy, 2005; Gao and Strowbridge, 2009). Short-term synaptic plasticity has been observed at this synapse (Dietz and Murthy, 2005) along with spike-timing dependent long-term depression with the activation of both proximal inputs and distal dendrites (Gao and Strowbridge, 2009). Our evidence of matching GC and MC/TC structural plasticity in vivo, combined with our model showing structural plasticity being ideal for connecting MCs with similar response profiles, suggests that the dendrodendritic synapse may rely on structural plasticity to function in the network without requiring synaptic strength plasticity.

Due to the persistent influx of newborn neurons to the OB, the dendrodendritic synapse seems adapted to employ structural plasticity as a primary form of plasticity, consistent with this synapse having limited synaptic plasticity. We observed small protrusions rapidly extending and retracting from the dendritic shaft and off of pre-existing mushroom-like spines (Breton-Provencher et al., 2014), termed “spinules,” in various brain regions

(Schuster et al., 1990). These protrusions suggest a regular sampling of the local environment as a potential form of synaptic competition (Spacek and Harris, 2004). In contrast to the neocortex or hippocampus where silent synapses provide a reservoir of new potential functional connectivity, dendrodendritic synapses have comparatively few silent members (Balu et al., 2007). Instead, by using a large search radius around a dendrite, the extensive spine dynamics may enable efficient remapping in the sparsely connected OB network, providing a larger number of potential synaptic partners than would be available to a neuron with a limited pool of silent synapses. Therefore, we would like to conclude that structural plasticity offers a more efficient mechanism in this context.

EXPERIMENTAL PROCEDURES

All experimental procedures followed approved guidelines regulated by institutional and national committees. Detailed methods are available in Supplemental Experimental Procedures. To express GFP in adult-born (P70) and early postnatal (P14) GCs, oncoretrovirus (Ubiquitin-C promoter-GPF-WPRE) was injected into the RMS/SVZ. To label MC/TC inhibitory synapses, Tbet-Cre mice (Haddad et al., 2013) were injected in the OB with floxed lenti-virus expressing a gephyrin-teal fusion (Ubiquitin-C-Teal-gephyrin) (Chen et al., 2012). Glass cranial windows 1.0 × 1.2 mm over each or one 3.0 × 1.4 mm window over both OB hemispheres were made and stainless steel head bar was cemented to the skull. Under isoflurane anesthesia (~0.8%), GCs were imaged with a Ti:Sapphire femtosecond pulsed laser (910 nm, Coherent) coupled to a LSM 510 microscope with a 20× 1.0 NA objective (Zeiss). Fluorescent-tagged gephyrin puncta were two-photon imaged (915 nm, Spectra Physics) with an Ultima microscope (Bruker) with a 25× 1.05 NA objective (Olympus).

Image Processing and Analysis

GCs were semiautomatically traced in 3D using Imaris software (Bitplane). Percent total spines were calculated as stable, $(100\times(N_{\text{stable spines}}/N_{\text{total spines}}))$; new, $(100\times(N_{\text{new spines}}/N_{\text{total spines}}))$; and lost, $(100\times(N_{\text{lost spines}}/N_{\text{total spines}}))$, where $N_{\text{total spines}} = N_{\text{stable spines}} + N_{\text{new spines}} + N_{\text{lost spines}}$. Data are presented as mean ± SEM. Statistical analysis was performed using one-way ANOVA with Origin software (OriginLab).

For the MC/TC puncta experiments, images were registered using affine and b-spline transformations, and dendritic segments were manually extracted. Puncta were automatically detected using Gaussian point detection, and puncta were linked between days if the fitted centroid moved less than a defined detection radius (1.44 μm unless otherwise specified). To count as new, puncta must have had at least two consecutive observations, and spines in Figure 6D also had this criterion applied.

Spine and Puncta Age Analysis

Spines and puncta whose formation (i.e., a frame where they were detected preceded by a frame where they were not detected) was observed were assigned the age *a* in units of interimaging intervals where *a* is the number of consecutive observations preceding the reference session. For Figures 7D and S7C, the frequencies of spines/puncta of a given age

were corrected for bias in favor of younger ages. For example, assuming a seven-session analysis window, age $a = 5$ can only be observed at the last session, whereas age $a = 0$ can be observed at any session except the very first. To simplify statistical analysis this correction was not applied to Figure S7B.

Computational Model of Spine Dynamics

The computational model is described in the Supplemental Experimental Procedures.

Supplementary Material

Refer to Web version on PubMed Central for supplementary material.

Acknowledgments

We thank Eileen Huang for data analysis; Soham Saha, Camille Mazo, Gabriel Lepousez, and Cyrille Norotte for manual puncta analysis; Dwight Bergels, David Linden, Randall Reed, Richard Huganir, and Chun Zhong for advice; Anne Lanjuin for providing Tbet-Cre mice; Elly Nedivi and Jerry Chen for providing the gephyrin-teal construct; and David DiGregorio for managing the Pasteur Institute Shared Neuroscience Department imaging facility funded by “Ile de France Domaine d’Intérê t Majeur (NeRF).” HPC Northwestern University provided HPC access (Quest). Support was provided by the following: W.A. and J.C.D., NSF undergraduate support RTG DMS-0636574; K.A.S., P.M.L., M.T.V., and M.T.W., “AG2R-La-Mondiale” life insurance, Agence Nationale de la Recherche ANR-15-CE37-0004-01, NIH US-French Research Proposal Grants #1R01DC015137-01 and ANR-15-NEUC-0004 (Circuit-OPL), the Laboratory for Excellence “Revive” Program (Investissement d’Avenir, ANR-10-LABX-73) and “Biopsy” (Investissement d’Avenir, ANR-11-IDEX-0004-02); K.A.S., NIH NRSA F31NS066612 and “Revive” fellowships; M.T.V., Pasteur-Roux fellowship and the Phillippe Foundation. H.J.S., NIH R37NS047344; G.L.M., NIH R01MH105128 and NIH R01NS048271, and the authors acknowledge the joint participation by the Diana Helis Henry Medical Research Foundation through its direct engagement in the continuous active conduct of medical research in conjunction with The Johns Hopkins Hospital and the Johns Hopkins University School of Medicine and the Foundation’s Parkinson’s Disease Program (No. H-1).

References

Adam Y, Mizrahi A. Long-term imaging reveals dynamic changes in the neuronal composition of the glomerular layer. J Neurosci. 2011; 31:7967–7973. [PubMed: 21632918]

Alonso M, Lepousez G, Sebastien W, Bardy C, Gabellec M-M, Torquet N, Lledo P-M. Activation of adult-born neurons facilitates learning and memory. Nat Neurosci. 2012; 15:897–904. [PubMed: 22581183]

Alvarez-Buylla A, Lim DA. For the long run: maintaining germinal niches in the adult brain. Neuron. 2004; 41:683–686. [PubMed: 15003168]

Attardo A, Fitzgerald JE, Schnitzer MJ. Impermanence of dendritic spines in live adult CA1 hippocampus. Nature. 2015; 523:592–596. [PubMed: 26098371]

Balu R, Pressler RT, Strowbridge BW. Multiple modes of synaptic excitation of olfactory bulb granule cells. J Neurosci. 2007; 27:5621–5632. [PubMed: 17522307]

Bannai H, Lévi S, Schweizer C, Inoue T, Launey T, Racine V, Sibarita JB, Mikoshiba K, Triller A. Activity-dependent tuning of inhibitory neurotransmission based on GABAAR diffusion dynamics. Neuron. 2009; 62:670–682. [PubMed: 19524526]

Bardy C, Alonso M, Bouthour W, Lledo P-M. How, when, and where new inhibitory neurons release neurotransmitters in the adult olfactory bulb. J Neurosci. 2010; 30:17023–17034. [PubMed: 21159972]

Bartel DL, Rela L, Hsieh L, Greer CA. Dendrodendritic synapses in the mouse olfactory bulb external plexiform layer. J Comp Neurol. 2015; 523:1145–1161. [PubMed: 25420934]

Bogdanov Y, Michels G, Armstrong-Gold C, Haydon PG, Lindstrom J, Pangalos M, Moss SJ. Synaptic GABAA receptors are directly recruited from their extrasynaptic counterparts. EMBO J. 2006; 25:4381–4389. [PubMed: 16946701]

Bourne JN, Harris KM. Nanoscale analysis of structural synaptic plasticity. Curr Opin Neurobiol. 2012; 22:372–382. [PubMed: 22088391]

Breton-Provencher V, Coté D, Saghatelyan A. Activity of the principal cells of the olfactory bulb promotes a structural dynamic on the distal dendrites of immature adult-born granule cells via activation of NMDA receptors. J Neurosci. 2014; 34:1748–1759. [PubMed: 24478357]

Cane M, Maco B, Knott G, Holtmaat A. The relationship between PSD-95 clustering and spine stability in vivo. J Neurosci. 2014; 34:2075–2086. [PubMed: 24501349]

Carleton A, Petreanu LT, Lansford R, Alvarez-Buylla A, Lledo P-M. Becoming a new neuron in the adult olfactory bulb. Nat Neurosci. 2003; 6:507–518. [PubMed: 12704391]

Chen JL, Villa KL, Cha JW, So PTC, Kubota Y, Nedivi E. Clustered dynamics of inhibitory synapses and dendritic spines in the adult neocortex. Neuron. 2012; 74:361–373. [PubMed: 22542188]

Chow S-F, Wick SD, Riecke H. Neurogenesis drives stimulus decorrelation in a model of the olfactory bulb. PLoS Comput Biol. 2012; 8:e1002398. [PubMed: 22442645]

De Paola V, Holtmaat A, Knott G, Song S, Wilbrecht L, Caroni P, Svoboda K. Cell type-specific structural plasticity of axonal branches and boutons in the adult neocortex. Neuron. 2006; 49:861–875. [PubMed: 16543134]

DeFelipe J. Types of neurons, synaptic connections and chemical characteristics of cells immunoreactive for calbindin-D28K, parvalbumin and calretinin in the neocortex. J Chem Neuroanat. 1997; 14:1–19. [PubMed: 9498163]

Dietz SB, Murthy VN. Contrasting short-term plasticity at two sides of the mitral-granule reciprocal synapse in the mammalian olfactory bulb. J Physiol. 2005; 569:475–488. [PubMed: 16166156]

Dobie FA, Craig AM. Inhibitory synapse dynamics: coordinated presynaptic and postsynaptic mobility and the major contribution of recycled vesicles to new synapse formation. J Neurosci. 2011; 31:10481–10493. [PubMed: 21775594]

Friedrich RW, Laurent G. Dynamic optimization of odor representations by slow temporal patterning of mitral cell activity. Science. 2001; 291:889–894. [PubMed: 11157170]

Friedrich RW, Wiechert MT. Neuronal circuits and computations: pattern decorrelation in the olfactory bulb. FEBS Lett. 2014; 588:2504–2513. [PubMed: 24911205]

Fusi S, Abbott LF. Limits on the memory storage capacity of bounded synapses. Nat Neurosci. 2007; 10:485–493. [PubMed: 17351638]

Fusi S, Drew PJ, Abbott LF. Cascade models of synaptically stored memories. Neuron. 2005; 45:599–611. [PubMed: 15721245]

Gao Y, Strowbridge BW. Long-term plasticity of excitatory inputs to granule cells in the rat olfactory bulb. Nat Neurosci. 2009; 12:731–733. [PubMed: 19412165]

Gonçalves JT, Bloyd CW, Shtrahman M, Johnston ST, Schafer ST, Parylak SL, Tran T, Chang T, Gage FH. In vivo imaging of dendritic pruning in dentate granule cells. Nat Neurosci. 2016; 19:788–791. [PubMed: 27135217]

Graziadei GA, Graziadei PP. Neurogenesis and neuron regeneration in the olfactory system of mammals. II. Degeneration and reconstitution of the olfactory sensory neurons after axotomy. J Neurocytol. 1979; 8:197–213. [PubMed: 469573]

Grutzendler J, Kasthuri N, Gan WB. Long-term dendritic spine stability in the adult cortex. Nature. 2002; 420:812–816. [PubMed: 12490949]

Gschwend O, Abraham NM, Lagier S, Begnaud F, Rodriguez I, Carleton A. Neuronal pattern separation in the olfactory bulb improves odor discrimination learning. Nat Neurosci. 2015; 18:1474–1482. [PubMed: 26301325]

Haddad R, Lanjuin A, Madisen L, Zeng H, Murthy VN, Uchida N. Olfactory cortical neurons read out a relative time code in the olfactory bulb. Nat Neurosci. 2013; 16:949–957. [PubMed: 23685720]

Holtmaat AJGD, Trachtenberg JT, Wilbrecht L, Shepherd GM, Zhang X, Knott GW, Svoboda K. Transient and persistent dendritic spines in the neocortex in vivo. Neuron. 2005; 45:279–291. [PubMed: 15664179]

Holtmaat A, Bonhoeffer T, Chow DK, Chuckowree J, De Paola V, Hofer SB, Hübener M, Keck T, Knott G, Lee W-CA, et al. Long-term, high-resolution imaging in the mouse neocortex through a chronic cranial window. Nat Protoc. 2009; 4:1128–1144. [PubMed: 19617885]

Johnson BA, Leon M. Chemotopic odorant coding in a mammalian olfactory system. J Comp Neurol. 2007; 503:1–34. [PubMed: 17480025]

Karube F, Kubota Y, Kawaguchi Y. Axon branching and synaptic bouton phenotypes in GABAergic nonpyramidal cell subtypes. J Neurosci. 2004; 24:2853–2865. [PubMed: 15044524]

Kelsch W, Lin CW, Lois C. Sequential development of synapses in dendritic domains during adult neurogenesis. Proc Natl Acad Sci USA. 2008; 105:16803–16808. [PubMed: 18922783]

Knott GW, Holtmaat A, Wilbrecht L, Welker E, Svoboda K. Spine growth precedes synapse formation in the adult neocortex in vivo. Nat Neurosci. 2006; 9:1117–1124. [PubMed: 16892056]

Kopel H, Schechtman E, Groysman M, Mizrahi A. Enhanced synaptic integration of adult-born neurons in the olfactory bulb of lactating mothers. J Neurosci. 2012; 32:7519–7527. [PubMed: 22649230]

Lazarini F, Mouthon MA, Gheusi G, de Chaumont F, Olivo-Marin JC, Lamarque S, Abrous DN, Boussin FD, Lledo PM. Cellular and behavioral effects of cranial irradiation of the subventricular zone in adult mice. PLoS ONE. 2009; 4:e7017. [PubMed: 19753118]

Lee WCA, Chen JL, Huang H, Leslie JH, Amitai Y, So PT, Nedivi E. A dynamic zone defines interneuron remodeling in the adult neocortex. Proc Natl Acad Sci USA. 2008; 105:19968–19973. [PubMed: 19066223]

Lemasson M, Saghatelyan A, Olivo-Marin J-C, Lledo P-M. Neonatal and adult neurogenesis provide two distinct populations of newborn neurons to the mouse olfactory bulb. J Neurosci. 2005; 25:6816–6825. [PubMed: 16033891]

Lepousez G, Valley MT, Lledo P-M. The impact of adult neurogenesis on olfactory bulb circuits and computations. Annu Rev Physiol. 2013; 75:339–363. [PubMed: 23190074]

Livneh Y, Mizrahi A. Long-term changes in the morphology and synaptic distributions of adult-born neurons. J Comp Neurol. 2011; 519:2212–2224. [PubMed: 21456001]

Livneh Y, Mizrahi A. Experience-dependent plasticity of mature adult-born neurons. Nat Neurosci. 2012; 15:26–28.

Livneh Y, Feinstein N, Klein M, Mizrahi A. Sensory input enhances synaptogenesis of adult-born neurons. J Neurosci. 2009; 29:86–97. [PubMed: 19129387]

Lledo P-M, Lagier S. Adjusting neurophysiological computations in the adult olfactory bulb. Semin Cell Dev Biol. 2006; 17:443–453. [PubMed: 16757194]

Lois C, Alvarez-Buylla A. Long-distance neuronal migration in the adult mammalian brain. Science. 1994; 264:1145–1148. [PubMed: 8178174]

Markram H, Toledo-Rodriguez M, Wang Y, Gupta A, Silberberg G, Wu C. Interneurons of the neocortical inhibitory system. Nat Rev Neurosci. 2004; 5:793–807. [PubMed: 15378039]

Mayford M, Siegelbaum SA, Kandel ER. Synapses and memory storage. Cold Spring Harb Perspect Biol. 2012; 4:a005751. [PubMed: 22496389]

Meier J, Vannier C, Sergé A, Triller A, Choquet D. Fast and reversible trapping of surface glycine receptors by gephyrin. Nat Neurosci. 2001; 4:253–260. [PubMed: 11224541]

Mizrahi A. Dendritic development and plasticity of adult-born neurons in the mouse olfactory bulb. Nat Neurosci. 2007; 10:444–452. [PubMed: 17369823]

Mizrahi A, Katz LC. Dendritic stability in the adult olfactory bulb. Nat Neurosci. 2003; 6:1201–1207. [PubMed: 14528309]

Mizrahi A, Lu J, Irving R, Feng G, Katz LC. In vivo imaging of juxtaglomerular neuron turnover in the mouse olfactory bulb. Proc Natl Acad Sci USA. 2006; 103:1912–1917. [PubMed: 16446451]

Moreno MM, Linster C, Escanilla O, Sacquet J, Didier A, Mandairon N. Olfactory perceptual learning requires adult neurogenesis. Proc Natl Acad Sci USA. 2009; 106:17980–17985. [PubMed: 19815505]

Mouret A, Gheusi G, Gabellec MM, de Chaumont F, Olivo-Marin JC, Lledo P-M. Learning and survival of newly generated neurons: when time matters. J Neurosci. 2008; 28:11511–11516. [PubMed: 18987187]

Mouret A, Lepousez G, Gras J, Gabellec MM, Lledo P-M. Turnover of newborn olfactory bulb neurons optimizes olfaction. J Neurosci. 2009; 29:12302–12314. [PubMed: 19793989]

Nusser Z, Cull-Candy S, Farrant M. Differences in synaptic GABA(A) receptor number underlie variation in GABA mini amplitude. Neuron. 1997; 19:697–709. [PubMed: 9331359]

Panzanelli P, Fritschy JM, Yanagawa Y, Obata K, Sassoè-Pognetto M. GABAergic phenotype of periglomerular cells in the rodent olfactory bulb. J Comp Neurol. 2007; 502:990–1002. [PubMed: 17444497]

Petreanu L, Alvarez-Buylla A. Maturation and death of adult-born olfactory bulb granule neurons: role of olfaction. J Neurosci. 2002; 22:6106–6113. [PubMed: 12122071]

Pomeroy SL, LaMantia AS, Purves D. Postnatal construction of neural circuitry in the mouse olfactory bulb. J Neurosci. 1990; 10:1952–1966. [PubMed: 2355260]

Rall W, Shepherd GM, Reese TS, Brightman MW. Dendrodendritic synaptic pathway for inhibition in the olfactory bulb. Exp Neurol. 1966; 14:44–56. [PubMed: 5900523]

Schuster T, Krug M, Wenzel J. Spinules in axospinous synapses of the rat dentate gyrus: changes in density following long-term potentiation. Brain Res. 1990; 523:171–174. [PubMed: 2207688]

Shepherd GM. Neuronal systems controlling mitral cell excitability. J Physiol. 1963; 168:101–117. [PubMed: 14056480]

Shepherd GM, Chen WR, Willhite D, Migliore M, Greer CA. The olfactory granule cell: from classical enigma to central role in olfactory processing. Brain Res Brain Res Rev. 2007; 55:373–382.

Somogyi P, Tamás G, Lujan R, Buhl EH. Salient features of synaptic organisation in the cerebral cortex. Brain Res Brain Res Rev. 1998; 26:113–135. [PubMed: 9651498]

Spacek J, Harris KM. Trans-endocytosis via spinules in adult rat hippocampus. J Neurosci. 2004; 24:4233–4241. [PubMed: 15115819]

Specht CG, Izeddin I, Rodriguez PC, El Beheiry M, Rostaing P, Darzacq X, Dahan M, Triller A. Quantitative nanoscopy of inhibitory synapses: counting gephyrin molecules and receptor binding sites. Neuron. 2013; 79:308–321. [PubMed: 23889935]

Sun GJ, Sailor KA, Mahmood QA, Chavali N, Christian KM, Song H, Ming G-L. Seamless reconstruction of intact adult-born neurons by serial end-block imaging reveals complex axonal guidance and development in the adult hippocampus. J Neurosci. 2013; 33:11400–11411. [PubMed: 23843512]

Triller A, Choquet D. Surface trafficking of receptors between synaptic and extrasynaptic membranes: and yet they do move! Trends Neurosci. 2005; 28:133–139. [PubMed: 15749166]

Tyagarajan SK, Fritschy J-M. GABA(A) receptors, gephyrin and homeostatic synaptic plasticity. J Physiol. 2010; 588:101–106. [PubMed: 19752109]

Valley MT, Mullen TR, Schultz LC, Sagdullaev BT, Firestein S. Ablation of mouse adult neurogenesis alters olfactory bulb structure and olfactory fear conditioning. Front Neurosci. 2009; 3:51. [PubMed: 20582278]

Valley MT, Henderson LG, Inverso SA, Lledo P-M. Adult neurogenesis produces neurons with unique GABAergic synapses in the olfactory bulb. J Neurosci. 2013; 33:14660–14665. [PubMed: 24027267]

van Versendaal D, Rajendran R, Saiepour MH, Klooster J, Smit-Rigter L, Sommeijer JP, De Zeeuw CI, Hofer SB, Heimel JA, Levelt CN. Elimination of inhibitory synapses is a major component of adult ocular dominance plasticity. Neuron. 2012; 74:374–383. [PubMed: 22542189]

Villa KL, Berry KP, Subramanian J, Cha JW, Oh WC, Kwon HB, Kubota Y, So PTC, Nedivi E. Inhibitory Synapses Are Repeatedly Assembled and Removed at Persistent Sites In Vivo. Neuron. 2016; 89:756–769. [PubMed: 26853302]

Whitman MC, Greer CA. Synaptic integration of adult-generated olfactory bulb granule cells: basal axodendritic centrifugal input precedes apical dendrodendritic local circuits. J Neurosci. 2007; 27:9951–9961. [PubMed: 17855609]

Whitman MC, Greer CA. Adult neurogenesis and the olfactory system. Prog Neurobiol. 2009; 89:162–175. [PubMed: 19615423]

Wick SD, Wiechert MT, Friedrich RW, Riecke H. Pattern orthogonalization via channel decorrelation by adaptive networks. J Comput Neurosci. 2010; 28:29–45. [PubMed: 19714457]

Wiechert MT, Judkewitz B, Riecke H, Friedrich RW. Mechanisms of pattern decorrelation by recurrent neuronal circuits. Nat Neurosci. 2010; 13:1003–1010. [PubMed: 20581841]

Winner B, Cooper-Kuhn CM, Aigner R, Winkler J, Kuhn HG. Long-term survival and cell death of newly generated neurons in the adult rat olfactory bulb. Eur J Neurosci. 2002; 16:1681–1689. [PubMed: 12431220]

Xu H-T, Pan F, Yang G, Gan W-B. Choice of cranial window type for in vivo imaging affects dendritic spine turnover in the cortex. Nat Neurosci. 2007; 10:549–551. [PubMed: 17417634]

Xu T, Yu X, Perlik AJ, Tobin WF, Zweig JA, Tennant K, Jones T, Zuo Y. Rapid formation and selective stabilization of synapses for enduring motor memories. Nature. 2009; 462:915–919. [PubMed: 19946267]

Yang G, Pan F, Gan WB. Stably maintained dendritic spines are associated with lifelong memories. Nature. 2009; 462:920–924. [PubMed: 19946265]

Yasumatsu N, Matsuzaki M, Miyazaki T, Noguchi J, Kasai H. Principles of long-term dynamics of dendritic spines. J Neurosci. 2008; 28:13592–13608. [PubMed: 19074033]

Zuo Y, Lin A, Chang P, Gan WB. Development of long-term dendritic spine stability in diverse regions of cerebral cortex. Neuron. 2005; 46:181–189. [PubMed: 15848798]

Highlights

- All granule cells in the olfactory bulb have highly dynamic spines throughout life
- Mitral/tufted cell gephyrin puncta have matching dynamics
- Computational modeling shows advantages of this robust structural plasticity
- Structural plasticity may be the primary form of plasticity at this synapse

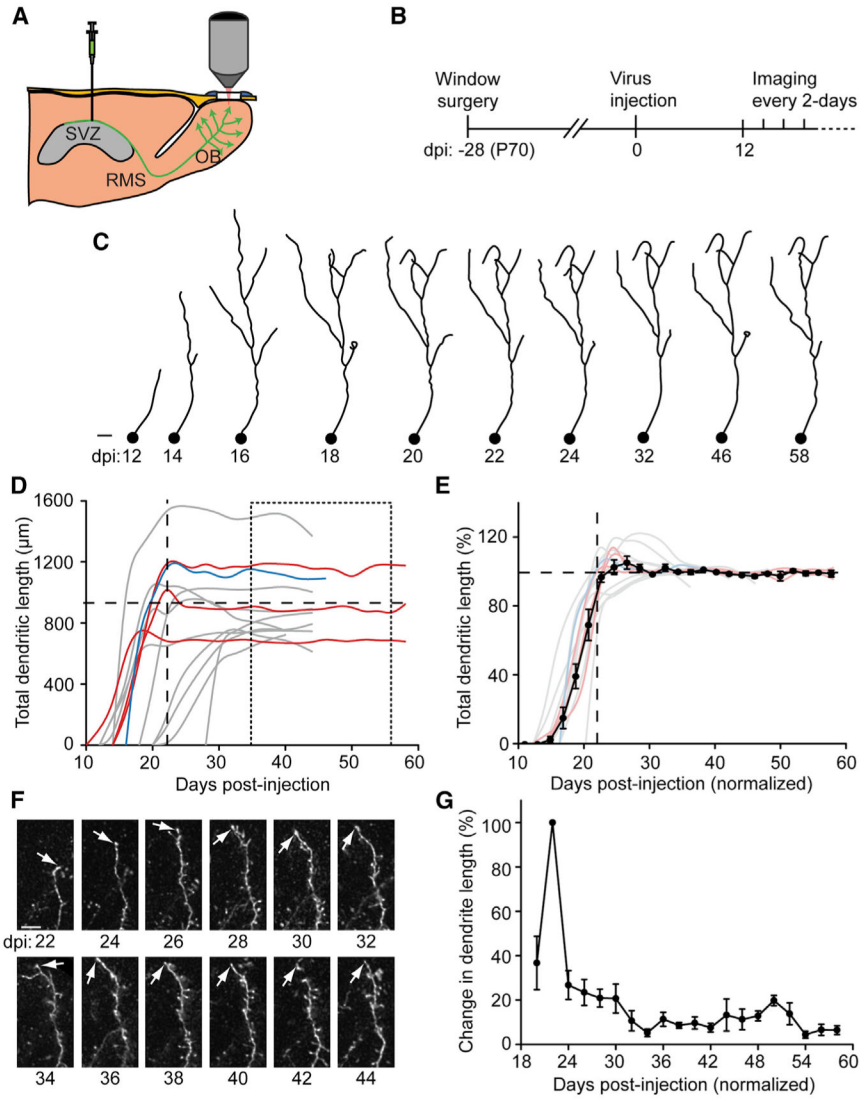

Figure 1. Development of Adult-Born GC Dendrites

(A) Cartoon of virus injection into the sub-ventricular zone (SVZ) to label adult-born neuroblasts that migrate via the rostral migratory stream (RMS) to the olfactory bulb (OB) becoming GCs that were two-photon imaged through a cranial window.

(B) Timeline was as follows: window surgery was performed 1 month prior to virus injection with the mice imaged at a 2-day interval starting at 12 days postinjection (dpi).

(C) 2D projections of 3D tracings of an adult-born GC from 12 dpi to 58 dpi. Scale bar, 20 μm.

(D) Plot of dendritic length of each traced GC (colors represent different animals). Horizontal long-dashed line: population total dendritic length average (902.9 ± 62.4 μm) taken between 36 to 58 dpi (short-dashed box). Vertical long-dashed line: average time of the initial dendritic growth plateau (23.2 ± 1.4 dpi).

(E) Individual tracings (color lines) and combined average dendritic length (black symbol-line) aligned to time at the dpi where the individual dendritic length initially plateaued and

each GC normalized to the saturated dendritic length (36 to 58 dpi individual GC average as 100%). Values represent mean ± SEM

(F) Example images of dendritic segments at a 2-day interval between 22 and 44 dpi. Scale bar, 10 μm.

(G) Plot of percent change in dendrite length (22 dpi = 100%) between 20 to 58 dpi. Values represent mean ± SEM.

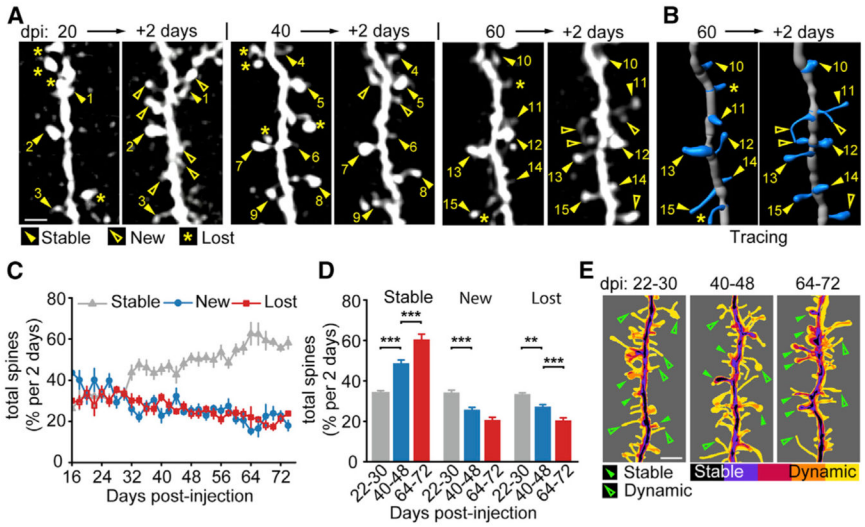

Figure 2. Adult-Born GC Developmental Spine Dynamics

(A) Sample images of the same adult-born GC dendritic segment at a 2-day interval for 20–22, 40–42, and 60–62 dpi showing stable (closed arrowheads with numbers indexing stable spines), new (open arrowheads), and lost (asterisks) spines.

(B) 3D tracings of the same 60–62 dpi segment as in (A). Scale bar, 4 μm.

(C) Plot of dynamics as percent of total average spines between 16–74 dpi with stable (gray triangles), new (blue circles) and lost (red squares) spines. Values represent mean ± SEM.

(D) Binned plots of 22–30, 40–48, and 64–72 dpi average spine dynamics at a 2-day interval. Values represent mean ± SEM. ANOVA, **$p < 0.05$, ***$p < 0.01$.

(E) Image-summed heatmap of five registered tracings of dendritic segments imaged at a 2-day interval overlaid for 22–30, 40–48, and 64–72 dpi ranges showing stable (closed arrowheads) and dynamic (open arrowheads) example spines. Scale bar, 4 μm.

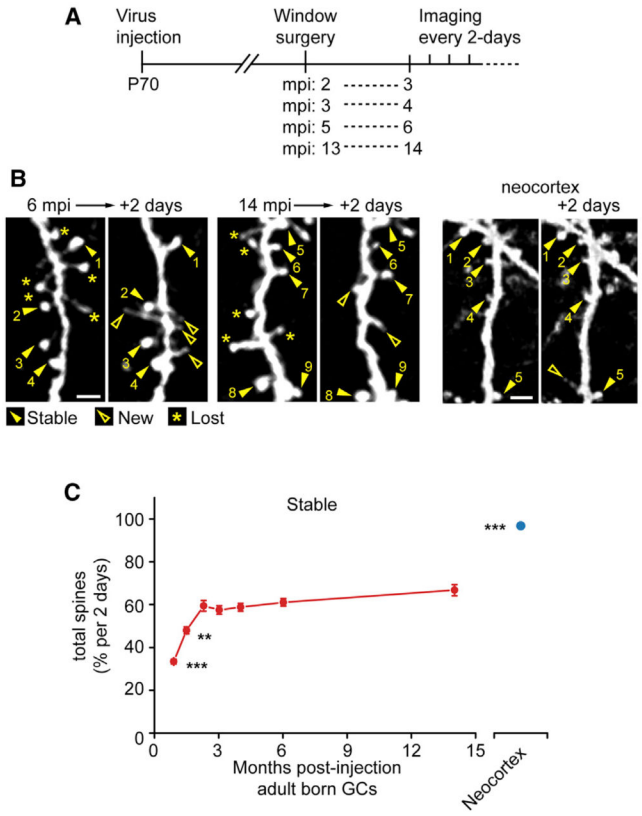

Figure 3. Long-Term Spine Dynamics of Adult-Born GCs

(A) Experimental timeline, mice were injected with virus at postnatal day 70 (P70), window surgeries following at 2, 3, 5, and 13 months postinjection (mpi) with 2-day interval imaging sessions beginning at 3, 4, 6, and 14 mpi, respectively.

(B) Sample images of GC dendritic segments at 6 and 14 mpi and of Thy-1-GFP-M mouse motor cortex pyramidal neuron dendritic spines with stable (closed arrowheads with numbers indexing stable spines) and new (open arrowheads) spines. Scale bar, 4 μm.

(C) Plot of 2-day interval spine stability of adult-born GCs (red circles, first three data points from Figure 2D) and neocortical pyramidal neurons (blue circle). Values represent mean ± SEM. ANOVA, **p < 0.05, ***p < 0.01.

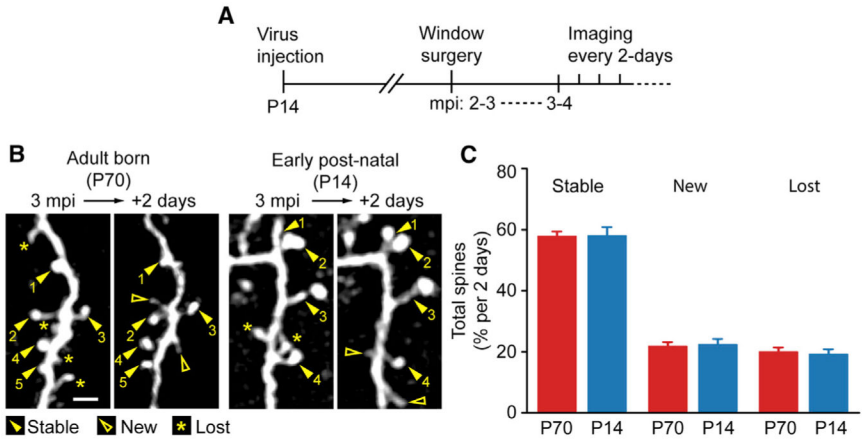

Figure 4. Adult-Born and Early Postnatal-Born GC Have Similar Spine Dynamics

(A) Experimental outline where early postnatal (P14) mice had virus injections followed by cranial window surgeries at 2–3 mpi and imaging at a 2-day interval at 3–4 mpi.

(B) Sample images of adult-born and early post-natal-born GC dendritic segments at a 2-day interval at 3 mpi with stable (closed arrowheads with numbers indexing stable spines), new (open arrowheads) and lost (asterisks) spines. Scale bar, 4 μm.

(C) Summary of spine dynamics between adult-born (P70, data from Figures 2D and 3C) and early postnatal-born (P14) groups at 3–4 mpi. Values represent mean ± SEM.

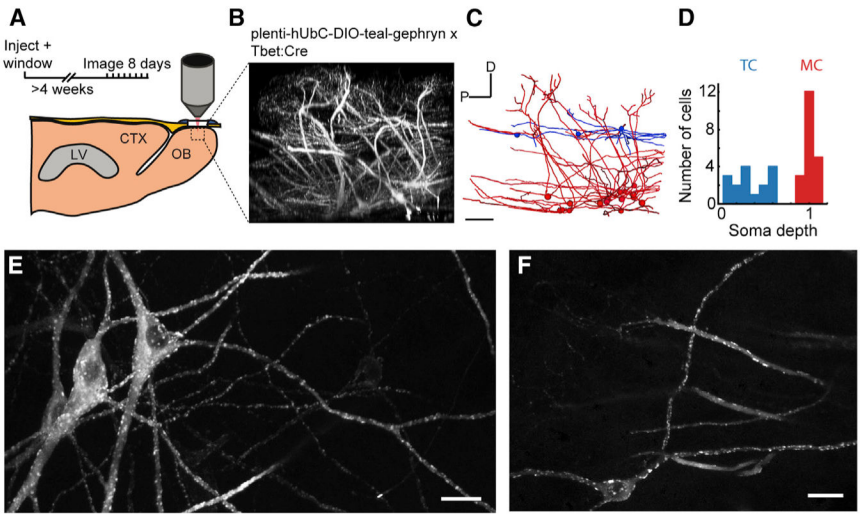

Figure 5. Imaging Teal-Gephyrin Puncta in Mitral and Tufted Cells

(A) Lentiviral injection of floxed-teal-gephyrin into the OB of adult Tbet-Cre mice was performed during the cranial window implantation procedure. Imaging began following a 4-week surgical recovery.

(B) 373 × 373 × ~250 μm (xyz) x-projected volume to show dorsal-ventral aspect of labeled mitral and tufted neurons. Scale bar, 50 μm.

(C) Morphological tracing of mitral (red) and tufted cells (blue). Scale bar, 50 μm.

(D) Classification of all tufted cells (TC) and mitral cells (MC) used in the study based on somatic depth referenced from the mitral cell layer (MCL). (E and F) Example z projections of in vivo imaged mitral cells (E), and tufted cells (F). Scale bar, 20 μm.

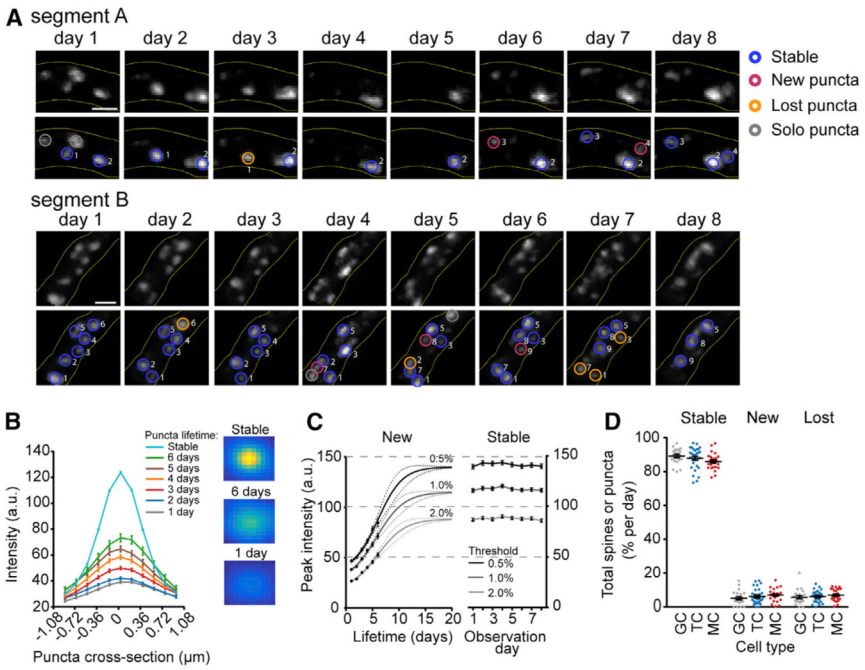

Figure 6. Loss of Both New and Stable Puncta Contributes to Similar Dynamics as GC Spines

(A) Example dendritic segments imaged at a 1-day interval, annotated to show examples of stable, new, lost puncta, and solo observations. Scale bar, 5 μm.

(B) Cross-sectional profiles (left) and representative images (right; one pixel = 0.182 μm) of average puncta from their first (gray), second (blue), third (red), fourth (orange), fifth (purple), sixth (green) observation, and the average profile of all stable puncta (teal).

(C) Logistic growth of puncta peak intensity after puncta appearance (left). Puncta were collected using three different thresholds of detection that considered peaks in the top 0.5%, 1.0%, and 2.0% of ranked pixel intensities. Intensity of stable puncta over eight days of observation (right). The maximum of the logistic fit in new puncta (left) was constrained using the average values at each threshold. Puncta intensities are represented as 8-bit absolute values (0–255 grayscale).

(D) Number of stable, new, and lost GC spines and MC and TC puncta at a 1-day interval, as a proportion of total observed spines and puncta (excluding solo observations).

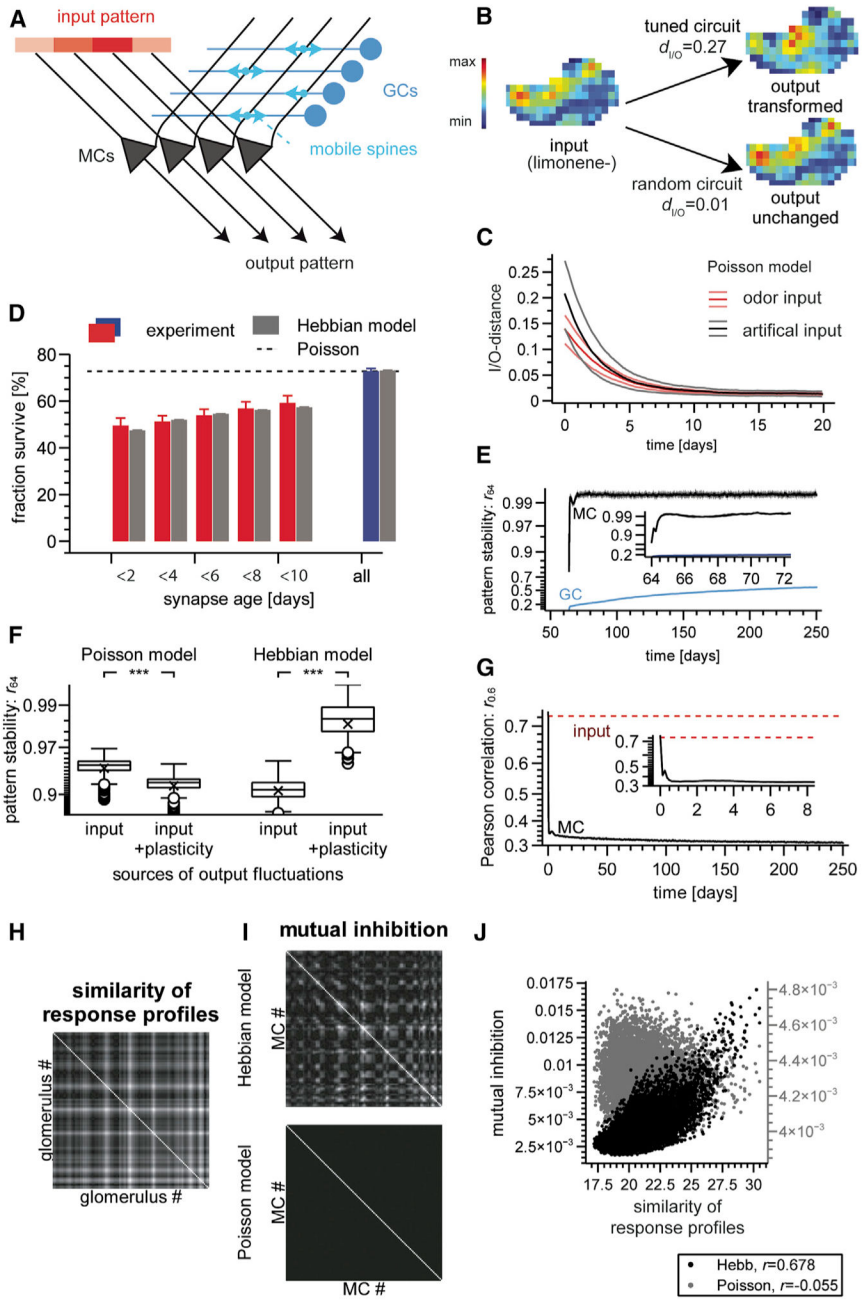

Figure 7. Modeling Functional Aspects of Synapse Turnover

(A) Schematic: two-population model of the OB; structural plasticity is modeled as rewiring of the connection matrix.

(B) Example of odor-evoked glomerular afferent response map used as model input (left) and evoked MC output maps generated by a structured (top right) and an unstructured (bottom right) circuit. $d_{I/O}$, I/O-distance.

(C) Degradation of circuit memory by Poisson synapse turnover quantified by I/O-distances of natural (black trace, mean ± SD, n = 26 networks × 24 stimuli) and of artificial inputs (red trace, mean ± SD, n = 26 networks × 12 stimuli). Initial circuit memory was created using

the Hebbian model described in the text. Artificially injected memory yielded similar results (Figure S7A).

(D) Spine-age dependent probability of a spine to survive until the next imaging session. Colored bars, experiment (mean ± SEM, n = 13 branches); gray bars, Hebbian model. Dashed line, matching Poisson model (all bars would have the same length).

(E) Stability of model responses quantified using Pearson correlation r_{64} between frames 64 days apart. Note nonlinear (Fisher z) y axis.

(F) Effect of spine plasticity on MC output stability for slowly fluctuating input. Box-and-whisker plots; boxes are delineated by quartiles 1–3, whiskers extend 1.5 times interquartile range, cross indicates mean and circles are outliers. Left two columns: Poisson model; input-induced fluctuations (left) are exacerbated (n = 24 odors × 12 networks; $p < 10^{-30}$; Wilcoxon rank sum test) by spine turnover (right). Right two columns: Hebbian model; input-induced fluctuations (left) are partially compensated for (n = 12 odors × 16 networks; $p < 10^{-30}$; Wilcoxon rank sum test) by spine turnover (right).

(G) Average pattern correlation $r_{0.6}$ between responses to related odors (input correlation $r > 0.6$) decreases with the exposure to these odors. Note non-linear (Fisher z) y axis. Inset, blow-up for early times.

(H) Overlap (scalar product) of response profiles between different input channels (“glomeruli”). Lighter intensity indicates higher overlap.

(I) Steady-state disynaptic MC-to-MC inhibition, excluding diagonal (self-inhibition). Lighter color indicates stronger weight.

(J) Same data (off-diagonal elements) as in (H) and (I). MCs associated with glomeruli with overlapping response profiles are preferentially connected ($r = 0.678$) in the Hebbian (black dots, left y axis) but not the Poisson (gray dots, right y axis) model. Parameters of computer model: $k_{MC} = 20$ synapses per GC, unitary synaptic weight $w = 8.125 \times 10^{-5}$. Poisson model only, probability of synapse replacement per update, 0.019. Hebbian model only, GC plasticity threshold $G_{min} = 16.0$, resilience threshold $R_0 = 1.015$, resilience threshold sharpness $\gamma = 50.0$, resilience update rate $\lambda_R = 0.01$.